Investigating Fracture in 3D Printed Plastic Parts in a Non-Laboratory Setting

Carter Cocke

ME EN 7530

May 1, 2021

Contents

1 Introduction and Background

In a recent market analysis report by Grand View Research [1], the 3D printing market size was valued at $11.6 billion and is expected to grow with a 14.6% compound annual growth rate (CAGR) to $35.4 billion by 2027. Additionally, the fused deposition modeling (FDM) plastics 3D printing subsector constituted the largest percentage of this market share. This rapid growth in plastics additive manufacturing (AM) necessitates more research into the mechanical response of 3D printed plastic parts. Given that 3D printed plastic parts are traditionally used for prototyping or hobbyist projects, this project aims to utilize a limited set of tools to better understand the fracture characteristics of 3D printed plastic parts. The primary objective of this work is to understand how cracks grow in 3D printed parts manufactured with varied print settings in order to gain insight into optimal build conditions. This work also aims to predict the critical mode 1 fracture toughness K_{I_c} through analytical and finite element analysis (FEA) methods. Finally, this work aims to utilize digital image correlation (DIC) to try and resolve the strain fields around a crack without a laboratory setup for comparison to FEA results. Through these three objectives, this work aims to give insight into the failure of 3D parts through at-home design, testing, and modeling.

2 Methods

2.1 PLA Material Properties

For this project, polylactic acid (PLA) filament was used as it is one of the most widely used 3D printing plastics. There are two material properties of PLA that make it excellent for fracture testing. Parts 3D printed with PLA are generally brittle with the total elongation of tensile coupons generally being less than 6% [2]. The brittle nature of PLA simplifies fracture modeling by satisfying a key assumption of linear elastic fracture mechanics (LEFM). Additionally, PLA also has an interesting visual/mechanical property in that it turns white in areas of large strains due to the amorphous polymer strands aligning themselves in the direction of large strains [3]. This color change allows for simple visualization of high strain areas around a crack tip (e.g., Figure 8a).

For subsequent coupon design and analysis, several material properties of PLA were required. It has been consistently shown that the mechanical properties of a 3D printed component are dependent on print settings, build configuration, and even PLA color [4–6]. It has, however, also been found that when specimens are only rotated on the build plate, material properties are generally not statistically different [4, 5]. The PLA filament used in this study was assumed to have the same properties as those in the literature. Table 1 gives a list of material properties for additively manufactured PLA at 100% and 50% internal infill percentages.

Table 1: Material properties of fused deposition modeling (FDM) polylactic acid (PLA). For material properties with multiple citations, a mean value from the sources is listed.

PLA Property	Infill 100%	Infill 50%	Units	Citation(s)
Elastic modulus, E	3.48	1.20	GPa	[5]
Poisson's ratio, ν	0.30			[7]
Yield strength, σ_{ys}	45.5	12.7	MPa	[5, 6]
Mode I fracture toughness, K_{I_c}	5.2		MPa$\sqrt{\text{m}}$	[5, 8, 9]
Mode II fracture toughness, K_{II_c}	3.6		MPa$\sqrt{\text{m}}$	[8]

2.2 Design of Test Coupons

2.2.1 Pre-Design Analysis

Given that samples were not tested in a laboratory environment with high-quality load frames, it was important to ensure that test coupons could be fractured using common household tools. In fact, supplying sufficient loads to fracture even small coupons turns out to be a significant hurdle using simple tensile forces. For example, consider the center cracked plate in Figure 1 loaded vertically with some remote stress, σ.

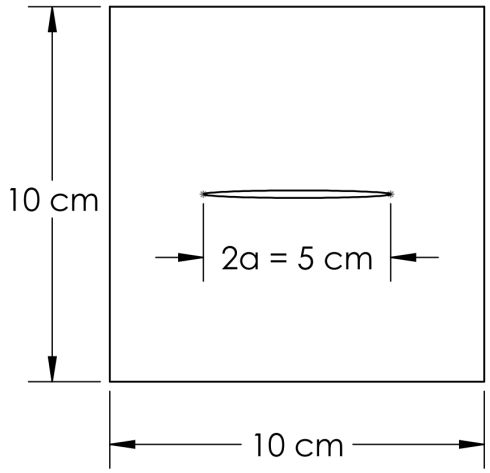

Figure 1: Example of a centered cracked plate with a 5 mm thickness.

The mode 1 stress intensity factor K_I of a finite center-cracked plate is defined as [10]:

$$K_{\text{I}} = \sigma\sqrt{\pi a}\left[1.0 + 0.128\left(\frac{a}{b}\right) - 0.288\left(\frac{a}{b}\right)^2 + 1.523\left(\frac{a}{b}\right)^3\right], \tag{1}$$

where a is the half-crack length of 2.5 cm and b is the half-plate width of 5 cm (with the 5 mm thick plate). Plugging in the cracked-plate geometry factor and solving for force, the following relation is obtained:

$$F_c = \frac{AK_{I_c}}{1.182\sqrt{\pi a}}, \tag{2}$$

where A is the cross-sectional area. Using the parameters from Table 1, the required force is $F_c = 7.8\,\text{kN}$. At this force, it would be impossible to manually exert enough force to grow the crack. Using this design, an impractically small part would need to be built to ensure the part could be broken by hand. To avoid these issues, a design that used bending (to leverage torque) or that could be gradually loaded without energy loss (i.e., forcing a wedge into the crack) was required.

2.2.2 Wedge Crack Growth Coupons

To simplify crack growth, a coupon was designed with an edge crack that would be forced open by hammering a wedge into the crack. The crack growth then becomes a displacement-controlled loading scenario in which the crack faces are separated. Figure 2 shows the two thin-plate geometries that were 3D printed. It is important to highlight that the cracks were printed directly into each coupon to emulate an actual crack in the material. Vălean et al. [8] showed that printing a notch directly into the part yields little difference in measured K_{I_c} values compared to milling a notch into the geometry. The specimens shown in Figure 2 were

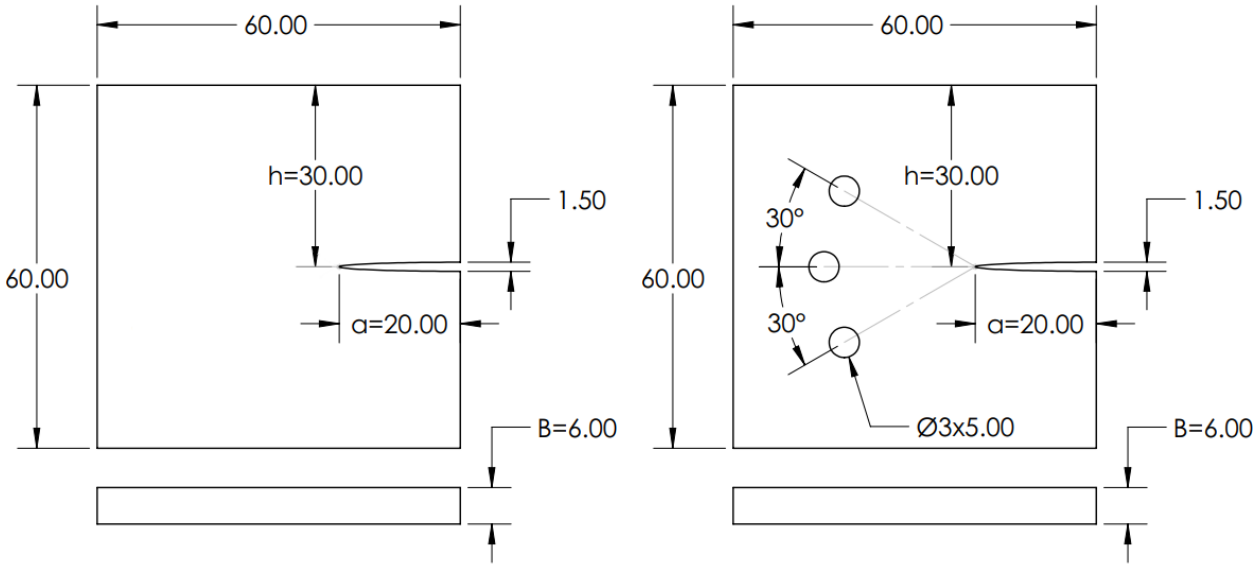

(a) Coupon with no holes.

(b) Coupon with holes.

Figure 2: Test coupons with a crack directly printed into the geometry (units in mm). In coupon (b), the holes are all equidistant (20 mm) from the crack tip at angles of $-30°$, $0°$, and $30°$.

loaded by hammering a 3D printed wedge into the crack. Hammering was performed with a force such that the wedge displacement slowly increased in order to mimic quasi-static loading as much as possible. The wedges were 3D printed scalene triangles with various aspect ratios printed at 100% infill to maximize stiffness. Some coupons required more displacement to grow the crack and thus required a larger wedge.

2.2.3 Print Setting Variation

To 3D print all test coupons, an Ender 3 Pro 3D printer was used. In this study, only internal infill density, internal infill type, and top/bottom layer infill type were varied. The same spool of black TECBEARS 1.75 mm PLA filament was used to print all test coupons. The main print settings used to print the coupons shown in Figure 2 using this filament are defined in Table 2.

Table 2: Print settings in Cura for all test coupons.

Print setting	Value	Units
Layer height	0.2	mm
Print speed	50	mm/s
Nozzle temperature	210	°C
Bed temperature	60	°C
Wall layers	3	
Top/bottom layers	5	

The top and bottom layer infill type was varied between the lines (default) and concentric infill types (see Figure 3). The internal infill type was varied between the lines (default), grid, triangle, and gyroid infill types in Cura (see Figure 4). Finally, the parts were printed with varied build directions between 0° and 90° on the build plate, as shown in Figure 5. Due to part reflectional symmetry, parts printed with a build orientation of n° were identical when printed with a build orientation of $(90 - n)$°, so the majority of parts were printed between 0° and 45°.

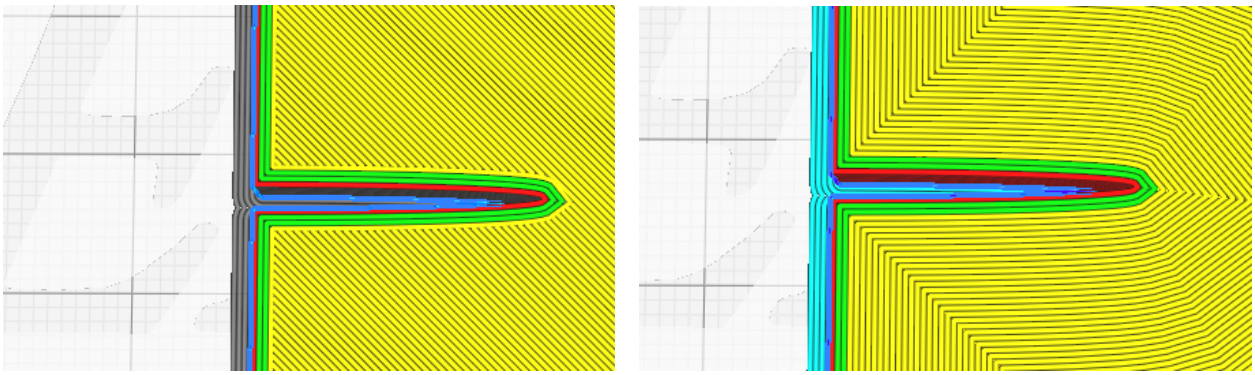

(a) Lines infill. **(b)** Concentric infill.

Figure 3: Top/bottom layer infill print settings used in Cura for test coupons.

Many combinations of the infill parameters and orientations shown in Figures 4–5 were chosen to print a total of 25 test coupons. The combinations of parameters chosen for each coupon are given in detail in the results section in Table 3 along with an approximation of the crack kink angle measured after part failure.

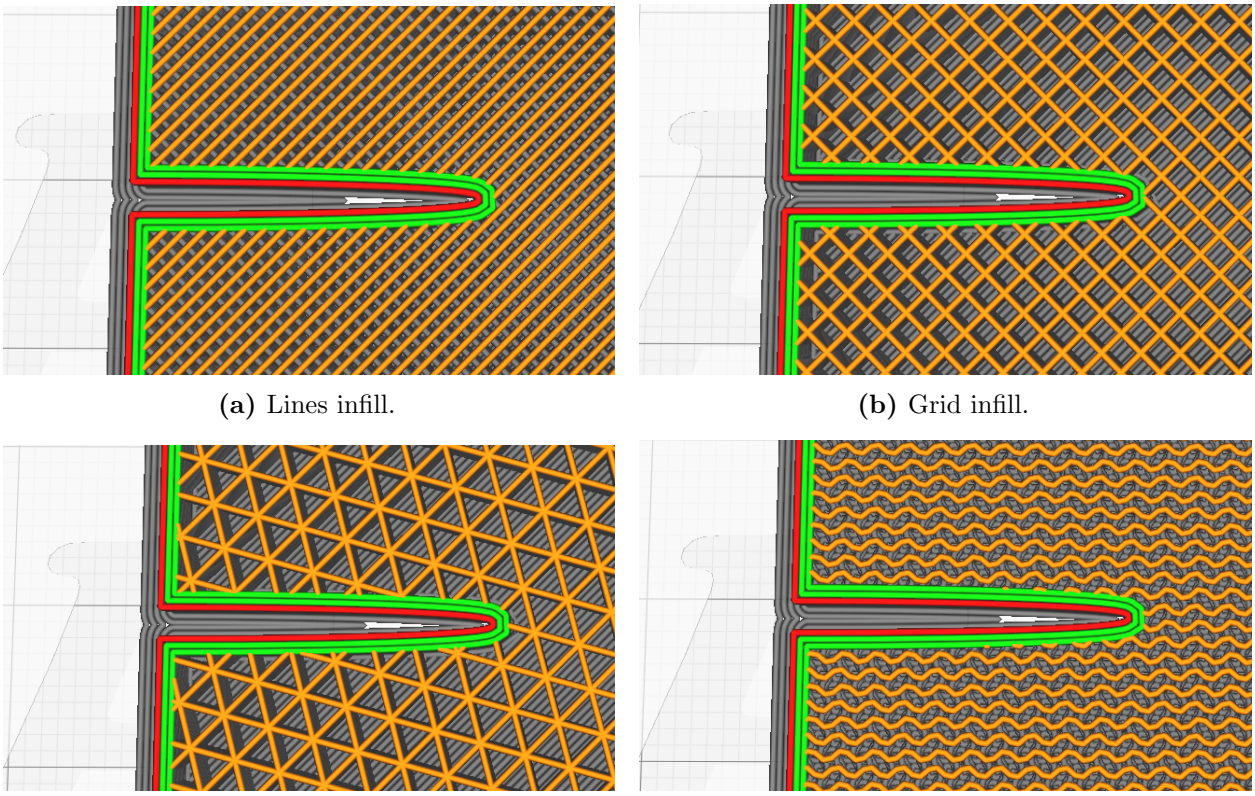

(a) Lines infill. **(b)** Grid infill.

(c) Triangle infill. **(d)** Gyroid infill.

Figure 4: Infill print settings used in Cura for test coupons.

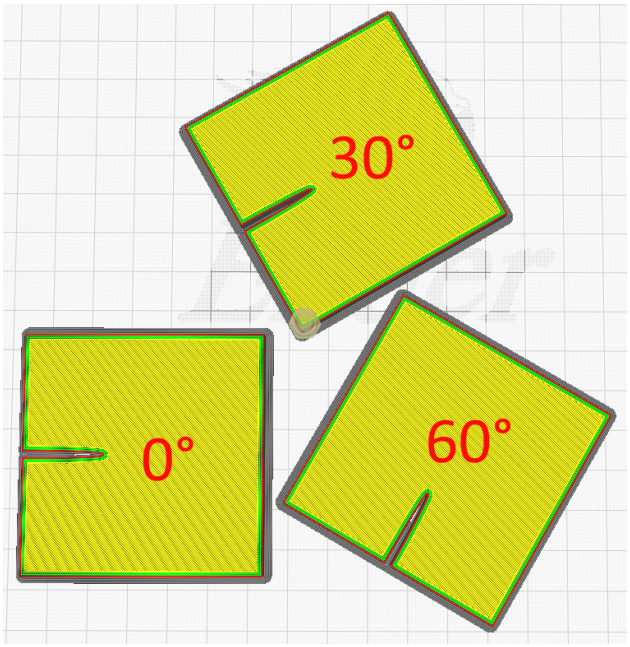

Figure 5: Example of three print bed orientations. Due to mirror symmetry in the part and infill, the 30° and 60° prints are effectively identical.

2.3 Analytical SIF Solution

Erdogan and Terada [11] derived an analytical solution for the displacement field of a semi-infinite strip force loaded with a rigid wedge. Unfortunately, the solution is extremely complex as it models the full displacement at the crack tip through a system of singular integrals. Additionally, the solution is for an applied force on the wedge rather than an applied displacement as in the wedge problem shown here. There are likely analytical displacement field solutions for double cantilever beam (DCB) geometries, but given that FEA can be used to solve for the fields it is not necessary to use an analytical solution. Instead, an analytical solution for K_I at the crack front of a DCB specimen can be used and compared to K_I calculated by FRANC3D. Using the Irwin-Kies relationship and the relationship between the energy release-rate G and stress intensity factor K, the analytical solution for the critical stress intensity factor K_{I_c} can be written as follows:

$$K_{I_c} = \sqrt{\frac{3E^2h^3\delta_c^2}{16a^4}}, \tag{3}$$

where h is the distance from the crack tip to the plate end, a is the crack length, E is the elastic modulus, and δ_c is the critical displacement. Equation 3 allows for K_{I_c} to be estimated by using the measured critical displacement at which the crack begins to propagate. The critical displacement δ_c was determined by experimentally measuring the average displacement at which the crack grew ($\delta_c \approx 1\,\text{mm}$) for several specimens using ImageJ. Due to the forced wedge testing setup, this displacement is only a very approximate guess for where the specimen failed.

2.4 Finite Element Analysis

FRANC3D and Abaqus were used to compute the stress intensity factors at the crack tip as well as the strain fields for comparison to experimental DIC results. Both plate geometries were imported and a small "true" crack with a length of 0.25 mm was inserted into the coupon ensuring that the template radius was small enough to extend beyond the crack embedded within the geometry. This means the FEA model had a crack that was slightly longer than the printed geometry, although given tolerances within the 3D printed part this had a negligible effect. The face opposite the crack front was fixed and an applied displacement of $\pm\delta_c$ was applied to both sides of the crack face to emulate the displacement caused by the forced wedge crack opening. The edges where the displacement was applied had significant deformation; however, these points were far enough away from the crack that the fields were able to smooth before the crack tip.

2.5 Digital Image Correlation

Four of the 25 printed coupons were analyzed using DIC. The coupons were spray painted using matte white spray paint to achieve a random speckle pattern that could be used with DIC software. For each coupon, images were taken with a cell phone camera before and during wedge insertion to analyze the progression of the strain field with increasing applied

displacement. The camera position was attempted to remain fixed with respect to the part. Figure 6 shows one of the coupons with the speckle pattern applied prior to loading.

Figure 6: Spray painted speckle pattern used for digital image correlation (DIC).

To analyze each image, the open-source DIC software Ncorr was used. For three coupons, a large subset radius of 120 pixels was used due to a lack of speckle patterns. This large subset radius results in a smoother strain field where small localized effects are smeared or not visible. For the final coupon, a subset radius of 40 pixels was used as the speckle pattern was denser. Lens distortion was not considered.

3 Results

3.1 Crack Paths

Figure 7 shows the 25 failed coupons arranged by print settings/geometry. The print settings of each coupon shown in Figure 7 are given in Table 3 with corresponding color grouping. Figure 8 shows a part printed with the concentric top/bottom infill setting both during loading and after total failure.

There are a few interesting fracture characteristics that were noticed during coupon testing. In the case where the 3D print layer lines were -45° and 45° from the crack tip, coupons initially failed gradually (semi-stable crack growth) with crack growth visible in some cases before sudden failure. In all cases where the layer lines were 0° and 90° from the crack tip, parts failed catastrophically with crack growth occurring all at once (i.e., unstable crack growth) with the part generally ejecting from the test location with high velocity (not seen in the -45° and 45° parts).

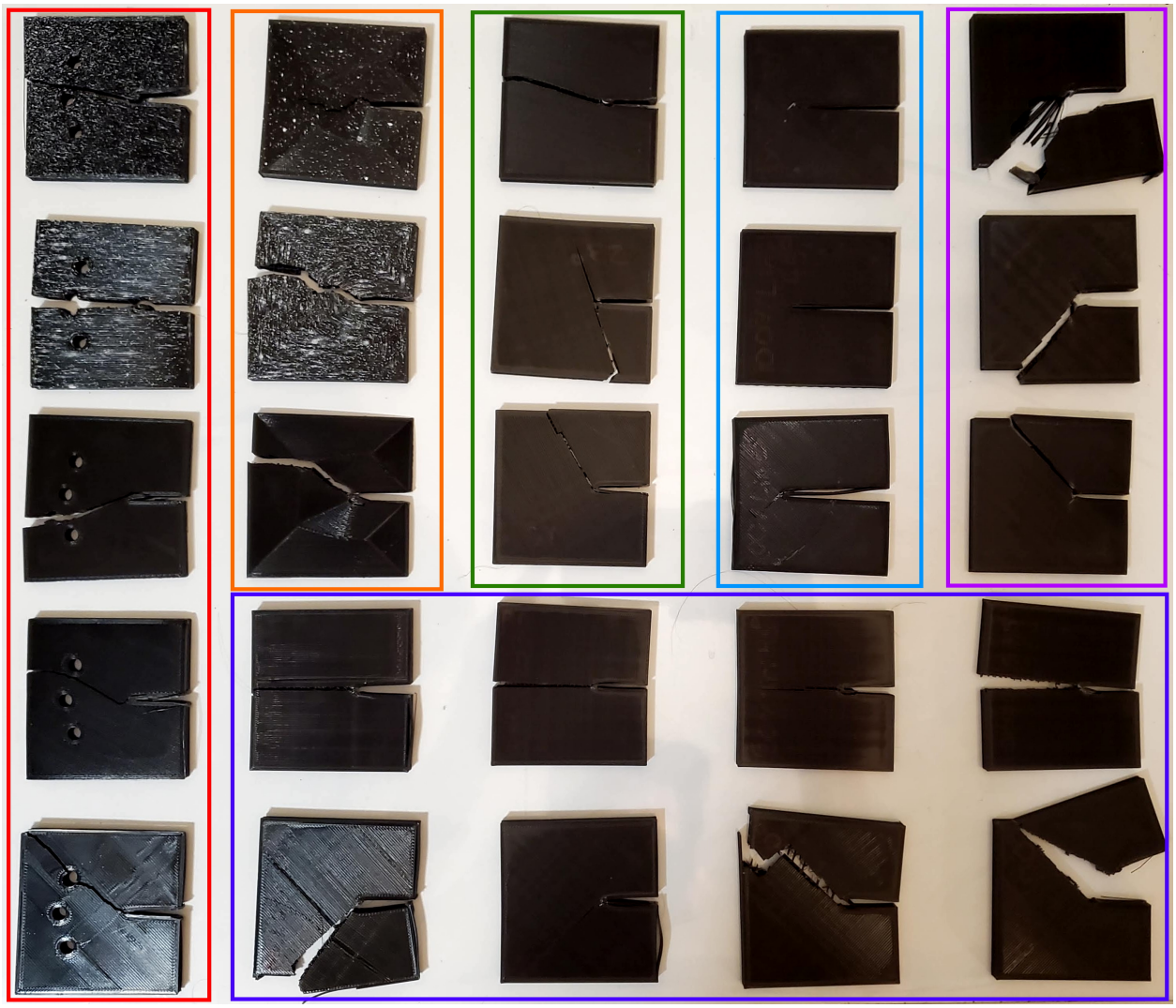

Figure 7: All 25 fracture coupons tested and sorted by print settings. ■ Coupons with holes printed at angles between 0° and 45°. ■ Coupons with concentric top/bottom infill printed at 0°, 23°, and 45°. ■ Coupons with line top/bottom infill printed at 15°, 23°, and 30°. ■ Coupons with a longer crack printed at 0°, 45°, and 90°. ■ Coupons with solid infill printed at 0° and 45°. ■ Coupons with varied infill type printed at 0° and 45°.

Table 3: Printing parameters and approximate average crack kink angle for all 25 coupons tested. The group column correlates with the colored boxes in Figure 7. The kink angle is given as an absolute value with a value of 0° indicating no kinking. Crack kink angle was estimated with ImageJ using the crack exit *if* the crack did not clearly propagate along layer lines with a known angle.

Group	Geometry	Orientation	Infill Parameters			Kink Angle
			Percent	Internal	Surface	
	Holes	30°	50%	Grid	Lines	9°
	Holes	45°	50%	Grid	Lines	0°
■	Holes	23°	50%	Grid	Lines	18°
	Holes	15°	50%	Grid	Lines	19°
	Holes	0°	50%	Grid	Lines	38°
	No Holes	45°	50%	Grid	Concentric	4°
■	No Holes	23°	50%	Grid	Concentric	12°
	No Holes	0°	50%	Grid	Concentric	19°
	No Holes	30°	50%	Grid	Lines	11°
■	No Holes	23°	50%	Grid	Lines	68°
	No Holes	15°	50%	Grid	Lines	57°
	Long Crack	90°	50%	Grid	Lines	45°
■	Long Crack	45°	50%	Grid	Lines	0°
	Long Crack	0°	50%	Grid	Lines	45°
	No Holes	0°	100%	Lines	Lines	41°
■	No Holes	0°	100%	Lines	Lines	49°
	No Holes	90°	100%	Lines	Lines	49°
	No Holes	45°	50%	Gyroid	Lines	0°
	No Holes	0°	50%	Gyroid	Lines	45°
	No Holes	45°	50%	Grid	Lines	0°
■	No Holes	0°	50%	Grid	Lines	45°
	No Holes	45°	50%	Triangle	Lines	0°
	No Holes	0°	50%	Triangle	Lines	45°
	No Holes	45°	100%	Triangle	Lines	0°
	No Holes	0°	100%	Triangle	Lines	45°

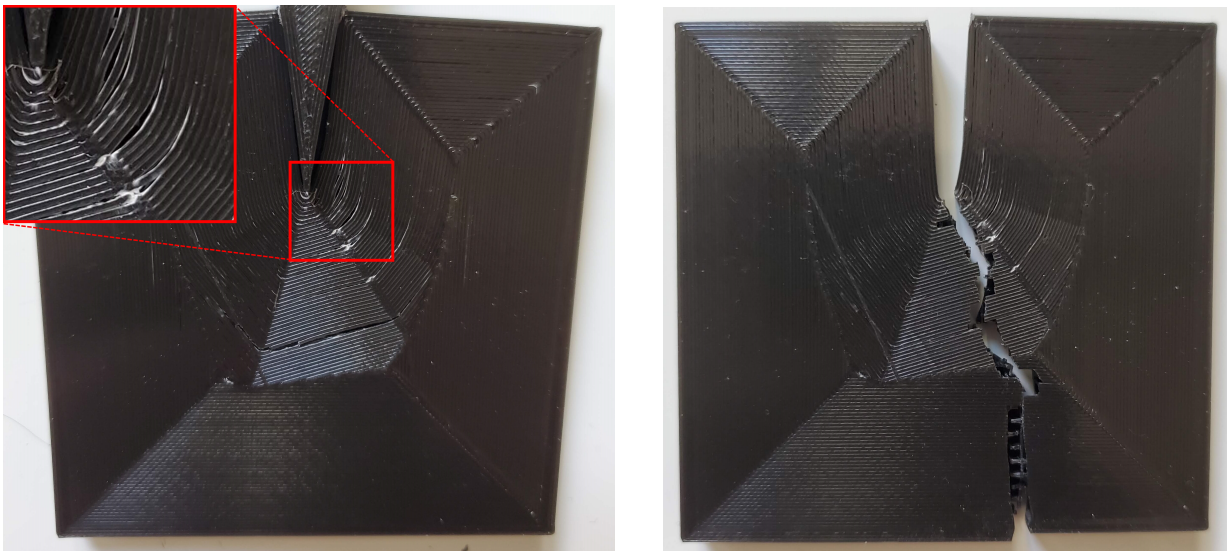

(a) Visible cracks during forced wedge loading. **(b)** Final crack path after failure.

Figure 8: Cracking during and after loading the concentric top/bottom layer infill coupon printed at 0°.

3.2 Critical Stress Intensity Factor

The critical stress intensity factors can be calculated through Equation 3 and through FRANC3D. Figure 9 shows the Von Mises and maximum absolute principal stress from the Abaqus FEA simulation of the coupon with no holes with a critical applied displacement of 1 mm. The average critical stress intensity factor at the crack tip as calculated by FRANC3D is $K_{I_c} = 1.78\,\text{MPa}\sqrt{\text{m}}$. The critical stress intensity factor as calculated by Equation 3 is $K_{I_c} = 6.75\,\text{MPa}\sqrt{\text{m}}$.

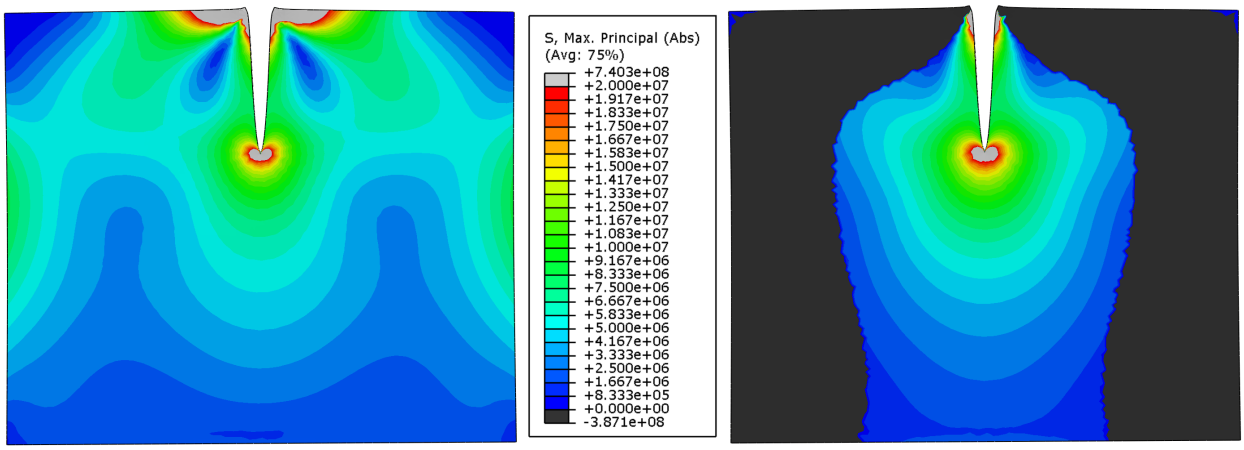

Figure 9: Von Mises stress (left) and maximum absolute principal stress (right) contour plots from the Abaqus/FRANC3D FEA simulation.

3.3 Digital Image Correlation

To analyze the effectiveness of the household DIC implementation, the strain fields calculated using Abaqus are compared to the strain fields computed using DIC. Figures 10 and 11 plots the E_{yy} and E_{xx} strain fields from DIC and Abaqus for the coupon with holes. This coupon had a subset radius of 40 pixels which is the smallest radius of all coupons tested (i.e., the highest strain field resolution). The color scales for each image are not necessary to compare as the DIC output has widely varied (incorrect) scales of strain.

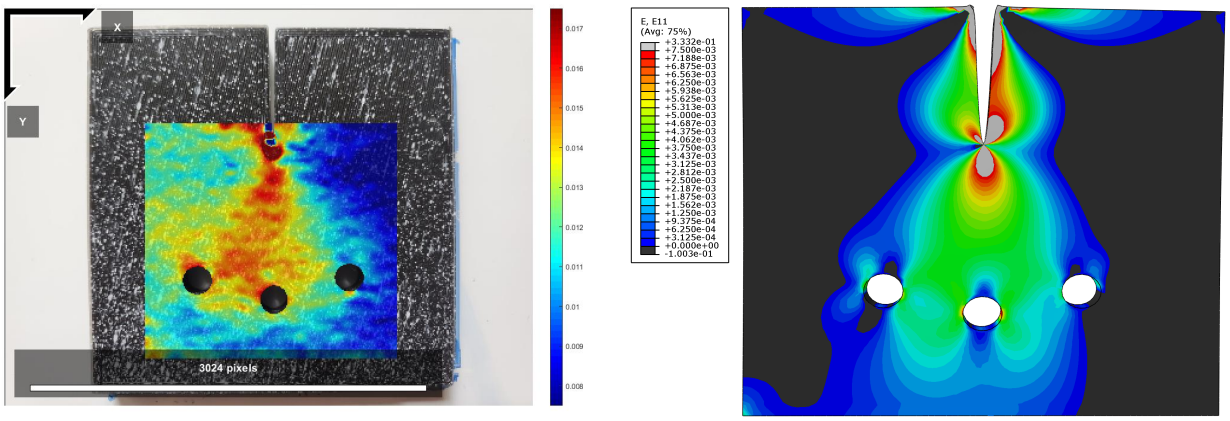

(a) DIC strain field. **(b)** Abaqus strain field.

Figure 10: E_{yy} (vertical) strain field comparison between DIC and Abaqus.

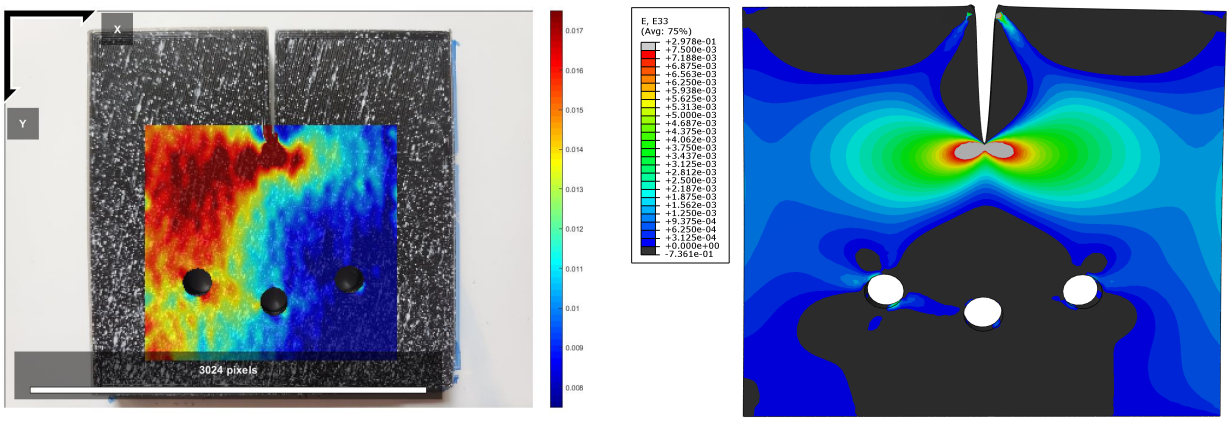

(a) DIC strain field. **(b)** Abaqus strain field.

Figure 11: E_{xx} (horizontal) strain field comparison between DIC and Abaqus.

4 Discussion

4.1 Crack Path

From the 25 coupons tested, there are a few takeaways that can be made for crack growth in 3D printed parts. The first is that cracks almost always tend to grow between top/bottom

layer lines regardless of the infill percentage or type. These observations held even when the concentric top/bottom infill type was used. During loading of a part with concentric top/bottom layer infill (Figure 8a), it can be seen that several microcracks exist between the layer lines radially outward from the crack tip. Once the part had completely failed (Figure 8b), it can be seen that the final crack path grew perpendicularly through the microcracks. Additionally, the final crack path grew perpendicular to the layer lines and turned to retain this perpendicular growth once the layer line orientations changed. In the case of the concentric top/bottom infill type (see Figure 3b), a much larger wedge was required to fail the coupon as all of the layer lines were perpendicular to the crack tip. This implies that the crack is easier to grow through layer lines rather than across them! With regard to internal infill parameters, there are other effects on fracture characteristics aside from the crack path. For example, when the infill percentage is lower, more displacement is required to fracture the coupons because the coupon is more compliant. Coupled with this, the type of infill used also affected the amount of displacement required with more randomly oriented infill types (e.g., the gyroid infill shown in Figure 4d) requiring more displacement to fail.

There are a few limitations to this study that require follow-up work to solidify gaps in the understanding of crack growth in 3D printed parts. All parts tested in this study were thin plates (1:10 thickness to width ratio) where the outer layers of the part constituted approximately 20% of the total thickness. For thicker parts, the internal infill parameters could have a larger impact; however, this was not tested as part of this work. More 3D printed geometries must be tested in order to understand if the observations seen in this work extend to more complicated shapes.

4.2 Critical Stress Intensity Factor

Comparing the experimental critical mode 1 stress intensity factors K_{I_c} calculated in Section 3.2 to the literature values given in Table 1, there are large discrepancies that are not unexpected. In general, the critical displacement of the wedge crack growth coupon results in SIF values that are within an order of magnitude from literature values. This is due to the difficulty in accurately measuring the displacement at which the crack begins to grow due to limitations in the testing method performed in this work. The largest limitation is that the displacement can only be measured before the part fails, which means the measured displacement will always be lower than the true displacement required to fail the part.

The analytical equation for K_{I_c} given in Equation 3 is based on Euler-Bernoulli beam theory which is not a very good model given the small length to width ratio of the beam. A better model would use a more advanced method such as Timoshenko beam theory. Regardless of this, the beam cross-section is not constant due to the non-zero distance between crack faces in the printed crack geometry, which only decreases the validity of analytical solutions. Due to these factors, the FEA simulation is likely much more accurate than the analytical solution, especially considering that the critical displacement is likely significantly understated (thus also understating K_{I_c}).

4.3 Digital Image Correlation

Comparing the FEA strain fields to the DIC strain fields shown in Figures 10 and 11, there are some interesting points to note. First, the DIC fields are relatively noisy. This is partially due to the small subset radius used in addition to speckle pattern and camera issues. However, the strain fields do correlate relatively well to the FEA results, at least qualitatively. The DIC strain scales are incredibly inaccurate and sensitive to camera position, but the gradients within the fields themselves do have a good amount of correlation. These results show that even without a laboratory DIC setup, strain fields can be qualitatively gauged, especially if some issues in the DIC setup were resolved.

The main issues with the DIC setup in this work can be split into two portions. The first being the camera and the second being the speckle pattern. With respect to the camera, a fixed mounting system for both the part and the camera is necessary to avoid strain field measurement inconsistencies between images. With respect to the speckle pattern, care is required to remove paint bleed into the layer lines as well as creating a speckle pattern that is roughly 50% dense. This could potentially be resolved by spray painting the part solid white followed by manually adding speckles using a permanent marker [12]. This would solve the issue of paint bleeding into the layers, but could potentially be too nonrandom. Alternatively, this could also be achieved by first spray painting a base white coat followed by a speckled black coat, but this remains untested.

5 Conclusions

Given the recent surge in consumer and industrial 3D printing, there is a need to better understand how 3D printed parts fail. The work presented in this report gives a broad understanding of 3D printed part failure that can be used as a basis for more in-depth future studies. Based on the previously presented work, the following conclusions can be made:

- Print settings are a key determining factor in the path a crack takes through a failed part. Cracks tend to propagate between layer lines and take paths that are as parallel or perpendicular to the layer lines as possible. Additionally, infill type has little effect on crack path but does influence part compliance and type of failure (stable versus unstable crack growth). In general, infill types that reduce the number of layer lines parallel to the crack tip are more resistant to crack growth.

- Critical stress intensity factors can be very roughly estimated through a wedge crack growth coupon; however, a need for more accurate displacement control and measurement is required to improve parameter estimates.

- Digital image correlation can be used in a non-laboratory setting with spray paint to get the strain fields in a crack testing coupon that are somewhat comparable to FEA simulations, especially in areas of large strains (i.e., at crack tips). More camera and speckle pattern control is required to get accurate strain measurements and a higher measurement resolution.

References

[1] Grand View Research. *3D Printing Market Size, Share & Trends Analysis Report By Material, By Component (Hardware, Services), By Printer Type (Desktop, Industrial), By Technology, By Software, By Application, By Vertical, And Segment Forecasts, 2020 - 2027*. Tech. rep. 978-1-68038-000-2. Feb. 2020, p. 250.

[2] Kyoung-SU Seol et al. "Infill Print Parameters for Mechanical Properties of 3D Printed PLA Parts". In: *The Korean Society of Manufacturing Process Engineers* 17 (Aug. 2018), pp. 9–16. DOI: 10.14775/ksmpe.2018.17.4.009.

[3] Chamil Abeykoon, Pimpisut Sri-Amphorn, and Anura Fernando. "Optimization of fused deposition modeling parameters for improved PLA and ABS 3D printed structures". In: *International Journal of Lightweight Materials and Manufacture* 3.3 (2020), pp. 284–297. DOI: https://doi.org/10.1016/j.ijlmm.2020.03.003.

[4] Jason Cantrell et al. "Experimental Characterization of the Mechanical Properties of 3D Printed ABS and Polycarbonate Parts". In: *Advancement of Optical Methods in Experimental Mechanics, Volume 3*. Ed. by Sanichiro Yoshida, Luciano Lamberti, and Cesar Sciammarella. Cham: Springer International Publishing, 2017, pp. 89–105.

[5] Adnan A. Ahmed and Luca Susmel. "Static assessment of plain/notched polylactide (PLA) 3D-printed with different infill levels: Equivalent homogenised material concept and Theory of Critical Distances". In: *Fatigue & Fracture of Engineering Materials & Structures* 42.4 (2019), pp. 883–904. DOI: https://doi.org/10.1111/ffe.12958.

[6] Ben Wittbrodt and Joshua M. Pearce. "The effects of PLA color on material properties of 3-D printed components". In: *Additive Manufacturing* 8 (2015), pp. 110–116. DOI: https://doi.org/10.1016/j.addma.2015.09.006.

[7] Andrew M. Baker et al. "Testing and simulation of thermal and mechanical properties of additively manufactured parts using fused deposition modelling (FDM)". In: (July 2018). URL: https://www.osti.gov/biblio/1463519.

[8] Cristina Vălean et al. "The effect of crack insertion for FDM printed PLA materials on Mode I and Mode II fracture toughness". In: *Procedia Structural Integrity* 28 (2020). 1st Virtual European Conference on Fracture - VECF1, pp. 1134–1139. DOI: https://doi.org/10.1016/j.prostr.2020.11.128.

[9] Florian Arbeiter et al. "Fracture mechanical characterization and lifetime estimation of near-homogeneous components produced by fused filament fabrication". In: *Polymer Testing* 66 (2018), pp. 105–113. DOI: https://doi.org/10.1016/j.polymertesting.2018.01.002.

[10] E. E. Gduotos. *Fracture Mechanics: An Introduction*. Springer Nature, 2005.

[11] Fazil Erdogan and Hiroaki Terada. "Wedge loading of a semi-infinite strip with an edge crack". In: *International Journal of Fracture* 14 (1978), pp. 399–415. DOI: https://doi.org/10.1007/BF00015992.

[12] Xiaowei Feng and Fei Xue. "Characterization of 3D printed bolts based on digital image correlation and infrared thermography". In: *Materials & Design* 191 (2020), p. 108641. DOI: https://doi.org/10.1016/j.matdes.2020.108641.